



Investigation of eddy diffusivity and heat transfer coefficient for free-falling turbulent liquid films subjected to sensible heating



Nikhin Mascarenhas, Issam Mudawar*

Purdue University Boiling and Two-Phase Flow Laboratory (PU-BTFFL), School of Mechanical Engineering, 585 Purdue Mall, West Lafayette, IN 47907, USA

ARTICLE INFO

Article history:

Received 10 March 2013
Received in revised form 24 April 2013
Accepted 25 April 2013
Available online 29 May 2013

Keywords:

Falling film
Eddy diffusivity
Film thickness
Heat transfer coefficient

ABSTRACT

The primary objective of this study is to develop a numerical model for turbulent, free-falling liquid films subjected to sensible heating. The model is used to explore the influences of waves and interfacial dampening of turbulent eddies on fluid flow and heat transfer. The model represents two-dimensional axisymmetric film flow on a vertical circular tube, with both the computational domain and operating conditions matching those of an experimental database for water films. Interfacial waves are observed to be prevalent for all operating conditions and associated with a dominant repeated wave shape. Good agreement is achieved between the predicted axial variations of the heat transfer coefficient and experimental data, including an upstream decline in the upstream thermal development region, and slow downstream increase resulting from intensified turbulence and interfacial waviness. Predicted relations for both the film thickness and heat transfer coefficient are shown to agree well with popular experimental correlations. It is shown that turbulence is fully suppressed at the interface, with zero eddy diffusivity both at the wall and interface, and a maximum in between.

© 2013 Elsevier Ltd. All rights reserved.

1. Introduction

Falling liquid films are found in a vast number of thermal systems, including condensers, evaporators, spray-type refrigerators, distillation columns, chemical reactors, and nuclear reactors. These films are typically thin, gravity-driven with negligible interfacial shear, and exhibit turbulent flow. The pioneering study by Nusselt [1] that culminated in an analytical model for heat transfer in laminar falling films has served as foundation for numerous studies spanning over nine decades concerning the prediction of heat transfer in both laminar and turbulent films undergoing cooling, condensation, sensible heating, and evaporation. Nusselt's model is strictly applicable to smooth, laminar films, which are encountered only at very low Reynolds number $Re = 4\Gamma/\mu < 33$ [2]. It is therefore not suited for films found in practical thermal systems, where high Reynolds numbers are desired to achieve high heat transfer rates. Accurate modeling of high Reynolds number films must account for turbulent fluctuations across the film. This is achieved with the aid of models for eddy momentum diffusivity, ε_m , and eddy heat diffusivity, ε_h , which are related to the shear stress and heat flux across the film, respectively, by

$$\tau = \rho(\nu + \varepsilon_m) \frac{\partial \bar{u}}{\partial y} = \mu \left(1 + \frac{\varepsilon_m}{\nu} \right) \frac{\partial \bar{u}}{\partial y} \quad (1)$$

and

$$q'' = -(k + \varepsilon_h) \frac{\partial \bar{T}}{\partial y} = -k \left(1 + \frac{Pr}{Pr_t} \frac{\varepsilon_m}{\nu} \right) \frac{\partial \bar{T}}{\partial y} \quad (2)$$

where $Pr_t (= \varepsilon_m/\varepsilon_h)$ is the turbulent Prandtl number. Unfortunately, determining the eddy diffusivity profile for turbulent films is far more challenging than for conventional internal or external liquid flows. Three primary reasons for this difficulty are:

- (1) Dampening of turbulent eddies at the film interface due to surface tension,
- (2) Difficulty ascertaining the transitional characteristics of falling film flows, and
- (3) Complex influence of interfacial waves on turbulence eddies.

Interfacial dampening of turbulent eddies is unique to liquid–gas and liquid–vapor interfaces, and this phenomenon is not accounted for with conventional eddy diffusivity models. Interfacial dampening is complicated by the uncertainty in determining transitions between film flow regimes and especially by interfacial waves, evidenced by the characterizations of film flows into smooth-laminar for $Re_f < 30$, wavy-laminar for $30 < Re_f < 1800$, and turbulent for $Re_f > 1800$ [2].

* Corresponding author. Tel.: +1 765 494 5705; fax: +1 765 494 0539.

E-mail address: mudawar@ecn.purdue.edu (I. Mudawar).

URL: <https://engineering.purdue.edu/BTFFL> (I. Mudawar).

Nomenclature

A^+	constant in eddy diffusivity models	y	coordinate perpendicular to the wall
c_p	specific heat at constant pressure	y_i	thickness of viscous sublayer
C_μ	turbulence model constant	<i>Greek Symbols</i>	
$e_{i,j}$	strain rate tensor	α	thermal diffusivity
g	gravitational acceleration	β	dimensionless film thickness; $\beta = \delta^{+2/3}$
G_1, G_2	coefficients in Gimbutis [10] eddy diffusivity equation	Γ	mass flow rate per unit film width
h_H	heat transfer coefficient for sensible heating, $q''_w/(T_w - T_m)$	δ	film thickness
h_H^*	dimensionless heat transfer coefficient, $(h_H v^{2/3})/(k g^{1/3})$	ε	dissipation rate of turbulent kinetic energy
k	thermal conductivity; turbulent kinetic energy	ε_h	eddy heat diffusivity
K	Von-Karman constant	ε_m	eddy momentum diffusivity
Ka	Kapitza number, $Ka = (\mu^4 g)/(\rho \sigma^3)$	μ	dynamic viscosity
L	length of heated portion of test section	ν	kinematic viscosity
n	coefficient in Dukler's [5] eddy diffusivity function	ρ	density
n_j	unit normal vector on free interface	σ	surface tension
P	pressure	τ	shear stress
Pr	Prandtl number	<i>Subscripts</i>	
Pr_t	turbulent Prandtl number	<i>crit</i>	critical
q''	local heat flux normal to the wall	<i>i</i>	direction index
q''_w	wall heat flux	<i>j</i>	direction index
r	radial coordinate	<i>m</i>	mean
R_1, R_2	radii of curvature at free interface	<i>t</i>	turbulent
Re	Reynolds number	<i>w</i>	wall
s_{ij}	fluctuating component of strain rate tensor	<i>Superscripts</i>	
t	time	–	average component
T	temperature	+	dimensionless
t_i	unit tangential vector on free interface	'	fluctuating component
T_m	mean film temperature		
u	velocity		
u_*	friction velocity		
x	axial coordinate		

To simplify film modeling, authors often focus on fully developed falling film flow with a smooth interface and negligible inter-

facial shear. As shown in Fig. 1, momentum balance for the indicated control volume yields

$$\tau = \mu \left(1 + \frac{\varepsilon_m}{\nu} \right) \frac{d\bar{u}}{dy} = \rho g (\delta - y). \quad (3)$$

The momentum and energy relations are non-dimensionalized in terms of the friction velocity, $u_* = \sqrt{\tau_w/\rho} = \sqrt{g\delta}$, $y^+ = u_* y/\nu$, $\bar{u}^+ = \bar{u}/u_*$, and $\bar{T}^+ = \rho c_p u_* (\bar{T}_w - \bar{T})/q''_w$. These definitions reduce Eqs. (3) and (2), respectively, to

$$1 - \frac{y^+}{\delta^+} = \left(1 + \frac{\varepsilon_m}{\nu} \right) \frac{d\bar{u}^+}{dy^+} \quad (4)$$

and

$$\frac{q''}{q''_w} = \frac{1}{Pr} \left(1 + \frac{Pr}{Pr_t} \frac{\varepsilon_m}{\nu} \right) \frac{\partial \bar{T}^+}{\partial y^+}. \quad (5)$$

1.1. Falling-film momentum diffusivity models

Turbulent falling films are generally modeled by assuming negligible interfacial shear. And while earlier falling film eddy diffusivity models do not account for interfacial dampening, most recent models do incorporate this important influence. Yih and Liu [3] and Mudawar and El-Masri [4] published comprehensive summaries of earlier eddy diffusivity models for prediction of heat transfer in falling liquid films.

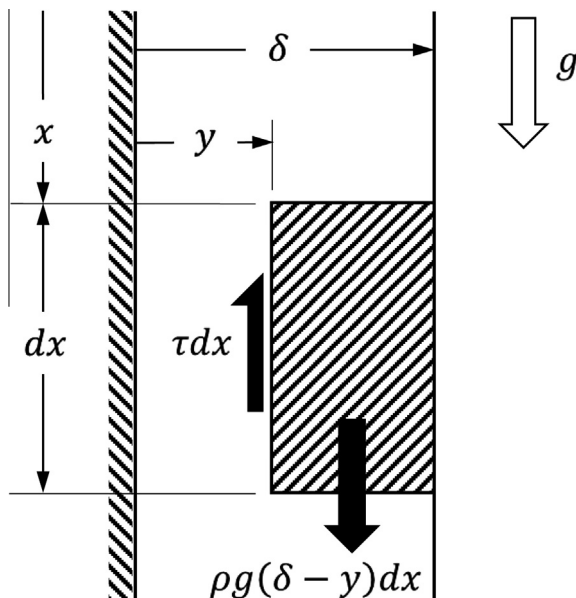


Fig. 1. Force balance for control volume of fully developed free-falling film.

Table 1
Eddy diffusivity models for freely falling films.

Author(s)	Model
Dukler (1960) [5]: $0 \leq y^+ \leq 20$ $20 < y^+$	$\frac{\varepsilon_m}{\nu} = n^2 u^+ y^+ [1 - \exp(-n^2 u^+ y^+)]$ $\frac{\varepsilon_m}{\nu} = K \left[\frac{du^+}{dy^+} \right]^3 \sqrt{\left[\frac{d^2 u^+}{dy^{+2}} \right]^2} \quad \text{Pr}_T = 1.0$
Iribarne et al. (1976) [6]: $0 \leq y^+ \leq \delta^+$	$\frac{\varepsilon_m}{\nu} = \frac{K}{12} \left[\exp(Ku^+) - 1 - Ku^+ - \frac{(Ku^+)^2}{2!} - \frac{(Ku^+)^3}{3!} \right] \quad K = 0.40$
Kunz and Yerazunis (1976) [7]: $0 \leq y^+ \leq \delta^+$	$\frac{\varepsilon_m}{\nu} = -\frac{1}{2} + \frac{1}{2} \sqrt{1 + 4K^2 y^{+2} \left(1 - \frac{y^+}{\delta^+}\right) \left(1 - \exp\left(-\frac{y^+}{A^+}\right)\right)^2}$ $\text{Pr}_T = 0.667 \exp\left\{\frac{-0.90}{(\frac{\varepsilon_m}{\nu})^{0.667}}\right\} \text{ (liquid metals)} \quad K = 0.40$
Mills and Chung (1973) [8]: $0 \leq y^+ < y_i^+$ $y_i^+ \leq y^+ < \delta^+$	$\frac{\varepsilon_m}{\nu} = -\frac{1}{2} + \frac{1}{2} \sqrt{1 + 4K^2 y^{+2} \left(1 - \exp\left(-\frac{y^+}{A^+}\right)\right)^2}$ $\frac{\varepsilon_m}{\nu} = 6.47 \times 10^{-4} Ka^{1/3} \frac{Re^{1.678}}{\delta^{+2/3}} (\delta^+ - y^+)^2 \quad \text{Pr}_T = 0.9 \quad K = 0.40; \quad A^+ = 26$
Limberg (1973) [9]: $0 \leq y^+ < 0.6\delta^+$ $0.6\delta^+ \leq y^+ < \delta^+$	$\frac{\varepsilon_m}{\nu} = -\frac{1}{2} + \frac{1}{2} \sqrt{1 + 4K^2 y^{+2} \left[1 - \exp\left\{\frac{-y^+ \left(1 - \frac{y^+}{\delta^+}\right)^{1/2}}{A^+}\right\}\right]^2 \left(1 - \frac{y^+}{\delta^+}\right) \exp(-3.32 \frac{y^+}{\delta^+})}$ $\frac{\varepsilon_m}{\nu} = \frac{\varepsilon_m}{\nu} \Big _{y^+=0.6\delta^+} \quad \text{Pr}_T = 0.89 \quad K = 0.41; \quad A^+ = 25.1$
Gimbutis (1974) [10]: $0 \leq y^+ < \delta^+$	$\frac{\varepsilon_m}{\nu} = -\frac{1}{2} + \frac{1}{2} \sqrt{1 + 4K^2 y^{+2} \left(1 - \frac{y^+}{\delta^+}\right) \exp\left\{\frac{-2(1 - \frac{y^+}{\delta^+})^{G_1}}{G_2}\right\}} \quad \text{Pr}_T = 0.9 \quad K = 0.40; \quad G_1 \text{ and } G_2 \text{ are empirical functions of } Re$
Ishigai et al. (1974) [11]: $0 \leq y^+ < \delta^+$	$\frac{\varepsilon_m}{\nu} = 0.1108K \left[\exp(Ku^+) - 1 - Ku^+ - \frac{(Ku^+)^2}{2!} - \frac{(Ku^+)^3}{3!} \right] \quad \text{Pr}_T = 1.0 \quad K = 0.40$
Seban and Faghri (1976) [12]: $0 \leq y^+ < 0.6\delta^+$ $0.6\delta^+ \leq y^+ \leq y_i^+$ $y_i^+ < y^+ \leq \delta^+$	$\frac{\varepsilon_m}{\nu} = -\frac{1}{2} + \frac{1}{2} \sqrt{1 + 4K^2 y^{+2} \left[1 - \exp\left\{\frac{-y^+ (1 - y^+ / \delta^+)^{1/2}}{A^+}\right\}\right]^2 (1 - y^+ / \delta^+) \exp(-3.32 y^+ / A^+)}$ $\frac{\varepsilon_m}{\nu} = \frac{\varepsilon_m}{\nu} \Big _{y^+=0.6\delta^+}$ $\frac{\varepsilon_m}{\nu} = 6.47 \times 10^{-4} Ka^{1/3} \frac{Re^{1.678}}{\delta^{+2/3}} (\delta^+ - y^+)^2 \quad \text{Pr}_T = 0.9 \frac{1 - \exp(-y^+ / A^+)}{1 - \exp(-\frac{y^+ (1 - y^+ / \delta^+)^{1/2}}{A^+})}; B^+ = f(\text{Pr}) \quad K = 0.40; \quad A^+ = 25.1$
Hubbard et al. (1976) [13]: $0 \leq y^+ < y_i^+$ $y_i^+ \leq y^+ < \delta^+$	$\frac{\varepsilon_m}{\nu} = -\frac{1}{2} + \frac{1}{2} \sqrt{1 + 4K^2 y^{+2} \left(1 - \frac{y^+}{\delta^+}\right) \left(1 - \exp\left(-\frac{y^+}{A^+}\right)\right)^2}$ $\frac{\varepsilon_m}{\nu} = \frac{8.13 \times 10^{-17} Re^{2m}}{Ka} (\delta^+ - y^+)^2$ $\frac{\varepsilon_m}{\nu} = 0.00661 Ka^{1/3} \frac{Re^{1.678}}{\delta^{+2/3}} (\delta^+ - y^+)^2 \quad \text{Pr}_T = 0.9, 1.0, 1.1 \quad K = 0.40; A^+ = 26; m = 695\nu^{1/2}, (\nu \text{ in m}^2/\text{s})$
Blangetti (1982) [14]: $0 \leq y^+ < y_i^+$ $y_i^+ \leq y^+ < \delta^+$	$\frac{\varepsilon_m}{\nu} = -\frac{1}{2} + \frac{1}{2} \sqrt{1 + 4K^2 y^{+2} \left(1 - \frac{y^+}{\delta^+}\right) \left(1 - \exp\left(-\frac{y^+}{A^+}\right)\right)^2}$ $\frac{\varepsilon_m}{\nu} = 0.00661 Ka^{1/3} \frac{Re^{1.678}}{\delta^{+2/3}} (\delta^+ - y^+)^2 \quad \text{Pr}_T = 0.9 \quad K = 0.40; \quad A^+ = 26; \quad \delta^+ = 0.169 Re^{2/3}$
Sandall et al. (1984) [15]: $0 \leq y^+ < y_i^+$ $y_i^+ \leq y^+ < \delta^+$	$\frac{\varepsilon_m}{\nu} = -\frac{1}{2} + \frac{1}{2} \sqrt{1 + \frac{4K^2 y^{+2} (1 - \exp(-\frac{y^+}{A^+}))^2}{1 - \exp(-0.26 \frac{y^+}{A^+})} (1 - y^+ / \delta^+)}$ $\frac{\varepsilon_m}{\nu} = 6.58 \times 10^{-4} Ka^{1/3} \frac{Re^{1.678}}{\delta^{+2/3}} (\delta^+ - y^+)^2 \quad \text{Pr}_T = 0.9 \quad K = 0.40; \quad A^+ = 26$
Mudawar and El-Masri (1986) [4]: $0 \leq y^+ \leq \delta^+$	$\frac{\varepsilon_m}{\nu} = -\frac{1}{2} + \frac{1}{2} \sqrt{1 + 4K^2 y^{+2} \left(1 - \frac{y^+}{\delta^+}\right)^2 \left[1 - \exp\left\{\frac{-y^+ \left(1 - \frac{y^+}{\delta^+}\right)^{1/2} \left(1 - \frac{0.865 Re^{1/2}}{\delta^{crit}}\right)}{A^+}\right\}\right]^2} \quad \text{Heating: } Re_{crit} = \frac{97}{Ka^{0.1}} \quad \text{Evaporation:}$ $Re_{crit} = \frac{0.04}{Ka^{0.27}} \quad \text{Pr}_T = 0.66 + 1.4 \exp\left\{-15 \frac{y^+}{\delta^+}\right\} \quad K = 0.40; \quad A^+ = 26$
Peterson et al. (1997) [16]: $0 \leq y^+ < 5$ $5 \leq y^+ < \frac{\delta^+}{2}$	$\frac{\varepsilon_m}{\nu} = 0.001 y^{+3} \quad \text{Pr}_T = 1.07$ $\frac{\varepsilon_m}{\nu} = -\frac{1}{2} + \frac{1}{2} \sqrt{1 + 4K^2 y^{+2} \left(1 - \frac{y^+}{\delta^+}\right)^2 \left(1 - \exp\left\{-\frac{y^+}{25} \left(1 - \frac{y^+}{\delta^+}\right)\right\}\right)^2} \quad \text{Pr}_T = 1 + 0.855 - \tanh\{0.2(y^+ - 7.5)\} \quad K = 0.40$
Alhusseini et al. (1998) [17]: $0 \leq y^+ < y_i^+$ $y_i^+ \leq y^+ < \delta^+$	$\frac{\varepsilon_m}{\nu} = -\frac{1}{2} + \frac{1}{2} \sqrt{1 + 4K^2 y^{+2} \left(\exp\left(-2.5 \frac{y^+}{\delta^+}\right)\right)^2 \left(1 - \exp\left(-\frac{y^+}{A^+}\right)\right)^2}$ $\frac{\varepsilon_m}{\nu} = \frac{1.199 \times 10^{-16} Re^{2m}}{Ka} \left(\frac{\delta^+ - y^+}{A_i^+}\right)^2$ $\text{Pr}_T = \frac{1}{0.581 + 0.216 Pe_t - (0.2 Pe_t)^2 \left\{1 - \exp\left(\frac{-1}{0.186 Pe_t}\right)\right\}} \quad K = 0.40; \quad A^+ = 26; \quad m = 3.49 Ka^{0.0675}; \quad A_i^+ = 0.01665 Ka^{-0.17324} \quad Pe_t = \left(\frac{\varepsilon_m}{\nu}\right) \text{Pr}$
Alhusseini and Chen (2000) [18]: $0 \leq y^+ < y_i^+$ $y_i^+ \leq y^+ < \delta^+$	$\frac{\varepsilon_m}{\nu} = -\frac{1}{2} + \frac{1}{2} \sqrt{1 + 4k^2 y^{+2} \left(\exp\left(-2.5 \frac{y^+}{\delta^+}\right)\right)^2 \left(1 - \exp\left(-\frac{y^+}{A^+}\right)\right)^2}$ $\frac{\varepsilon_m}{\nu} = \frac{1.199 \times 10^{-16} Re^{2m}}{Ka} \left(\frac{\delta^+ - y^+}{A_i^+}\right)^2$ $\text{Pr}_T = \frac{1}{1.72 + 0.2 Pe_t \sqrt{\frac{1}{0.36} - (0.2 Pe_t)^2} \left[1 - \exp\left(\frac{-1}{0.185 Pe_t}\right)\right]} \quad K = 0.40; \quad A^+ = 26; \quad m = 3.49 Ka^{0.0675}; \quad A_i^+ = 0.01665 Ka^{-0.17324} \quad Pe_t = \left(\frac{\varepsilon_m}{\nu}\right) \text{Pr}$
Asbik et al. (2005) [19]	

(continued on next page)

Table 1 (continued)

Author(s)	Model
$0 \leq y^+ \leq 5$	$\frac{\epsilon_m}{\nu} = 0$
$5 \leq y^+ \leq 70$	$\frac{\epsilon_m}{\nu} = \frac{y^+}{5} - 1$
$70 \leq y^+ \leq \delta^+$	$\frac{\epsilon_m}{\nu} = \frac{y^+}{2.5} - 1 \quad Pr_t = 0.9$

Table 2
Falling film thickness correlations.

Author(s)	Thickness correlation	Range
Brauer (1956) [30]:	$\beta = 0.208Re^{0.533}$	$1.7 \leq Re \leq 6800$
Gimbutis (1974) [10]:	$\beta = (0.0318Re^{0.92} + 8)^{2/3}$	$Re \leq 100,000$
Takahama and Kato (1980) [31]:	$\beta = 0.228Re^{0.526}$	$42 \leq Re \leq 997$
Karapantsios and Karabelas (1995) [32]:	$\beta = 0.217Re^{0.538}$	$370 \leq Re \leq 11,020$
Zhang et al. (2000) [33]:	$\beta = 1.442Re^{0.333}$	$Re \leq 2000$
	$\beta = 0.304Re^{0.583}$	$Re > 2000$
Ye et al. (2002) [34]:	$\beta = 0.295Re^{0.498}$	$400 \leq Re \leq 5000$

Table 1 provides a summary of popular falling film eddy diffusivity models. Earlier models were based largely on conventional formulations for external or internal liquid flows. Rohsenow et al. [20], for example, modified the *law of the wall* to develop the Prandtl–Nikuradse eddy diffusivity model. Dukler [5] used the eddy diffusivity model by Deissler [21], Iribarne et al. [6] the Spalding model [22], and Kunz and Yerazunis [7] the Van Driest model [23]. Most models were based on near-wall eddy diffusivity formulations, and, as such, required multiple functions to account for eddy diffusivity profile transitions from the wall to the outer layers, and an additional function to capture the influence of interfacial dampening. A key disadvantage in using multiple functions is the existence of discontinuities in the eddy diffusivity profile at the transition boundaries.

More recently, the Van Driest model [23] gained popularity for modeling the wall region of falling films, but required mathematical adjustment to tackle the interface region. Mills and Chung [8], Seban and Faghri [12], Hubbard et al. [13], and Mudawar and El-Masri [4] accounted for dampening of eddy diffusivity near the interface. Mudawar and El-Masri developed a single continuous eddy diffusivity profile incorporating the Van Driest model near the wall, an experimental profile derived from open channel data by Ueda et al. [24] for the bulk region of the film, and a dampening multiplier for the interface region using the treatments of Kays [25] and Kays and Crawford [26]. On the other hand, the eddy diffusivity of Alhuseini et al. [17] is comprised of a near-wall function by Limberg [9] and a Taylor series expansion using data by Won and Mills [27] for the interface. In their numerical study, Asbik et al. [19] employed the Von Karman model [28] after modifying the upper y^+ limit to 70 as recommended by Schlichting [29].

Several studies yielded specific correlations for film thickness and heat transfer coefficient for turbulent falling films undergoing sensible heating as shown in Tables 2 and 3, respectively. To both validate models and/or develop correlations for momentum and heat transfer in turbulent falling films, investigators relied on published databases such as those of Wilke [35], Gimbutis [10], Ganchev et al. [38], Gimbutis et al. [39], Shmerler and Mudawar [36,40], Lyu and Mudawar [41,42], Houpt and Mudawar [43,44], and Ye et al. [34]. A few studies culminated in simple relations for the heat transfer coefficient for fully developed turbulent films in terms of the Reynolds and Prandtl numbers as shown in Table 3. Lyu and Mudawar [41,42] and Houpt and Mudawar [43,44] also explored the influence of interfacial waves on the film flow.

The present study concerns the development of a numerical model for turbulent falling liquid films that are subjected to

sensible heating. The model is capable of predicting interfacial waves and accounting for interfacial dampening. The accuracy of the numerical predictions is assessed relative to a database for water spanning a broad range of Reynolds numbers. The numerical results are used to construct detailed eddy diffusivity profiles for different operating conditions, as well as simple dimensionless relations for both the film thickness and heat transfer coefficient.

2. Experimental methods

This study utilizes the Purdue University Boiling and Two-Phase Flow Laboratory (PU-BTPFL) database for falling films to assess the accuracy of computational predictions for water films subjected to sensible heating. As shown in Fig. 2(a), the film is formed on the outer surface of a vertical 25.4-mm diameter, 1835-mm long cylindrical test section. The test section is comprised of three parts: a 300-mm long inlet porous polyethylene tube, a 757-mm long G-10 fiberglass plastic tube, and a 781-mm long stainless steel tube. De-ionized water is supplied from a reservoir into the inside of the polycarbonate tube, and flows radially outwards through the porous wall before falling as a thin film downwards along the outer surface of the test section. With a mean porosity of 20 μm , the polyethylene tube causes the water film to be injected uniformly and with minimal radial velocity.

The middle, adiabatic G-10 tube enables the film flow to develop hydrodynamically before being subjected to sensible heating along the outer surface of the lower stainless steel tube. Soldered to the upper and lower ends of the stainless steel tube are connectors made from oxygen free copper, which serve as electric terminals. Heat is dissipated uniformly within the 0.41-mm thick stainless tube by supplying low voltage, high d.c. current (up to 15 volts at 750 amps) across the copper terminals. This produces a constant heat flux along the outer surface of the stainless tube. As shown in Fig. 2(a), the test section is mounted within a leak proof chamber made from Lexgard plastic. This chamber is made up of two identical flanged sections with outer dimensions of $152.5 \times 152.5 \times 991 \text{ mm}^3$ and a wall thickness of 35 mm.

Type-T thermocouples are used to measure inside temperatures of the stainless steel wall and the mean film temperatures. The wall temperature is measured at 17 axial locations by diametrically opposite thermocouple pairs. These pairs are more concentrated towards the top of the stainless steel tube to help capture thermal entrance effects. The bead of each inner wall thermocouple is embedded in a small mass of thermally conducting boron nitride epoxy that is deposited into the head of a 6–32 nylon socket

Table 3
Heat transfer coefficient correlations for falling films subjected to sensible heating.

Author(s)	Correlation	Range
Wilke (1962) [35]:	$h_H^* = 2.07Re^{-1/3}$ $h_H^* = 0.0323Re^{1/5}Pr^{0.344}$ $h_H^* = 0.00102Re^{2/3}Pr^{0.344}$ $h_H^* = 0.00871Re^{2/5}Pr^{0.344}$	$Re < 2460 Pr^{-0.646}$ $2460 Pr^{-0.646} < Re < 1600$ $1600 < Re < 3200$ $3200 < Re$
Gimbutis (1974) [10]:	$h_H^* = (0.165Re^{0.16} - 0.4)Pr^{0.34} \left[\frac{Pr}{Pr_w} \right]^{0.25}$	$5.4 < Pr < 210$ $2800 \leq Re \leq 70,000$
Shmerler and Mudawar (1988) [36]:	$h_H^* = 0.0106Re^{0.3}Pr^{0.63}$	$4.3 < Pr < 8.4$ $2500 \leq Re \leq 39,500$
Al-Najem et al. (1998) [37]:	$h_H^* = 6.832 \times 10^{-4} \left(Re^{0.4829} Pr^{0.93717} - \frac{21817.84}{Re} \right)$	$2.55 < Pr < 6.87$ $4000 \leq Re \leq 20,000$
Ye et al. (2002) [34]:	$h_H^* = 0.00462Re^{0.429}Pr^{1/3}$	$1.8 < Pr < 4.4$ $800 \leq Re \leq 7000$ $2.55 < Pr < 7.2$

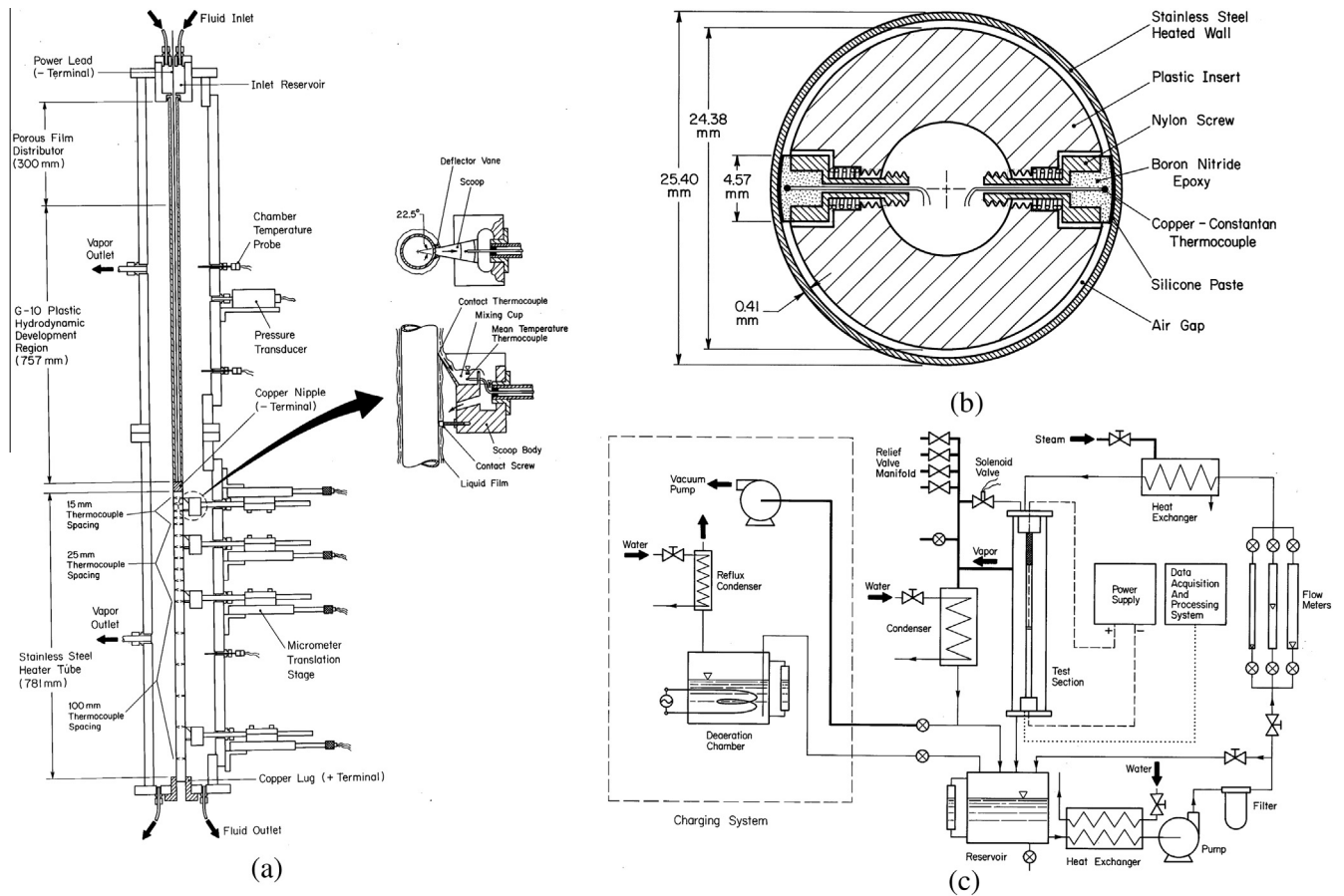


Fig. 2. (a) Cut-away view of test chamber. (b) Cross-sectional view of inner thermocouples. (c) Schematic diagram of flow loop.

head cap screw as shown in Fig. 2(b). The epoxy is machined to a cylindrical profile to match the inner surface of the stainless steel tube. The threads of the nylon screw closest to the head are machined out to insert a stainless steel spring, while a few threads on the opposite end of the screw are retained for insertion into a Delrin plastic tube that is slid along the inside of the stainless tube. This arrangement allows the screw to be compressed normal to the axis of the Delrin tube. During assembly, the screw heads are covered with thermally conducting silicone grease, then each diamet-

rically opposite pair is compressed inwards for insertion into the stainless steel tube. Once inserted, the springs force the screws outwards, ensuring that the boron nitride epoxy makes precise contact with the inner wall of the stainless steel tube. This process is repeated for each thermocouple pair as the Delrin tube is slid gradually through the stainless steel tube.

The mean film temperature is measured with the aid of sampling scoops made from G-10 plastic as shown in Fig. 2(a). Four such scoops are used along the heated length with each scoop

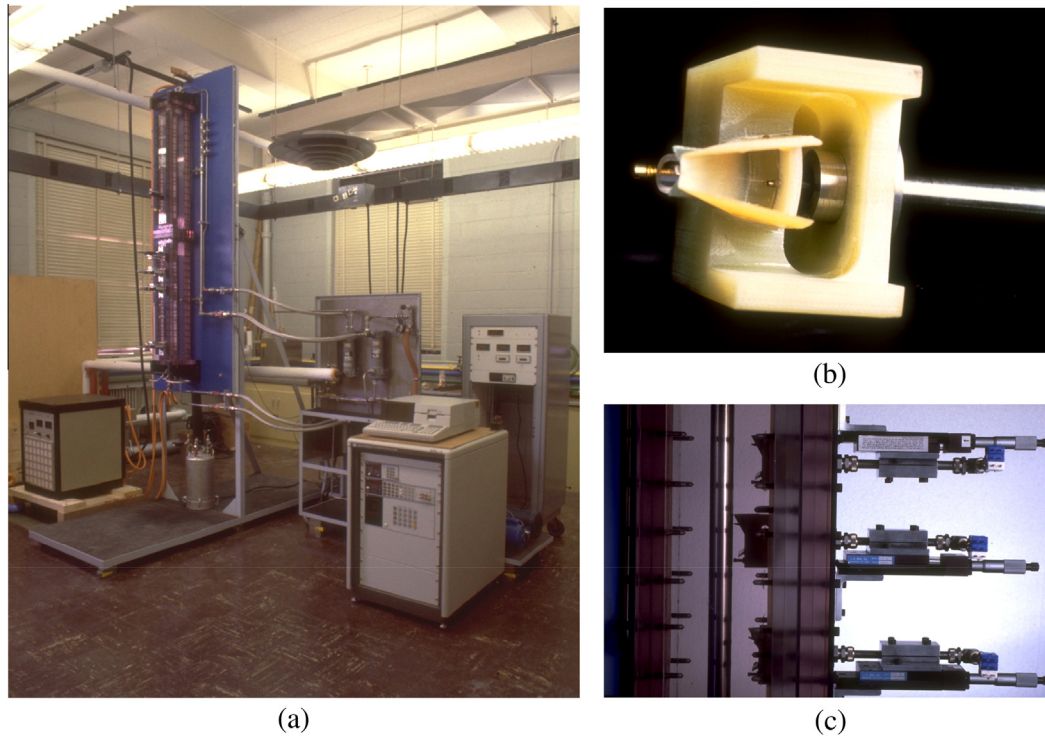


Fig. 3. Photos of (a) falling film facility, (b) top view of sampling scoop, and (c) stainless steel tube and sampling scoops mounted on micrometer stages.

location corresponding to one of the 17 inside wall measurement locations. Mean film temperatures between consecutive scoops are interpolated based on the scoop measurements and an energy balance between the two scoops. Each scoop is mounted on a micrometer translation stage, which allows the operator to advance or retract the scoop relative to the stainless steel tube. The curvature of the leading edge of the scoops is machined to match the outside curvature of the stainless steel tube, while the scoop sidewalls intersect the centerline of the tube at a 22.5° angle. As the scoop penetrates the film, the fluid is captured inside a mixing cup containing a thermocouple bead, which allows the measured temperature to conform to the standard definition of mean liquid temperature. To avoid flooding of the sampling cup or wall dry-out beneath, the sampled liquid is deposited back onto the heated wall. Another important feature of the sampling scoops is a copper screw that is aligned with the forward edge of the scoop. As the scoop is translated towards the stainless steel tube, proper placement is indicated once electrical contact is made between the copper screw and stainless steel tube. This also helps prevent exerting undue force that might buckle the stainless steel tube. One of the scoops is modified to determine the temperature profile by incorporating a small thermocouple bead into the leading edge of the scoop. This particular scoop is translated by a micrometer stage to different precise distances from the stainless steel tube to measure the temperature profile. It is important to emphasize that, because the scoop disrupts the film flow downstream, only one scoop is used at a given time while all three other scoops are retracted.

Fig. 2(c) shows a schematic diagram of the flow loop. Deionized water is first deaerated by vigorous boiling before being charged into the system. The water is then circulated through the loop at the desired flow rate, and the water temperature increased by steam flow through a heat exchanger situated upstream of the test section. Once the desired temperature at the test section inlet is reached, electrical power is supplied to the test section at a level that produces a $5\text{--}10^\circ\text{C}$ temperature rise across the film. The water

continues to be circulated at these conditions until the vapor surrounding the test section inside the test chamber reaches a temperature close to the film temperature at near-atmospheric pressure, and steady state conditions are achieved within the film.

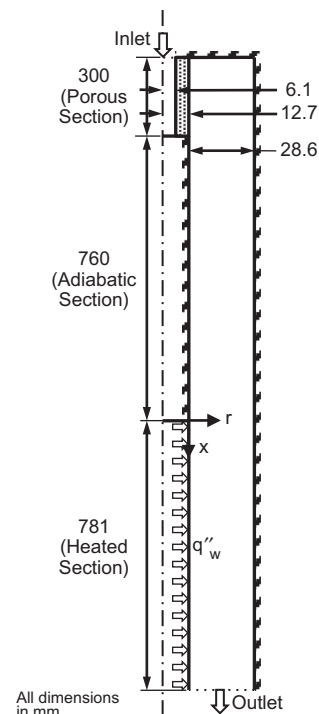


Fig. 4. Computational domain.

Table 4
Test cases and corresponding averaging time period for computations.

Re	Pr	Δt(s)
25680	3.56	0.07
25060	4.35	0.07
23970	2.55	0.07
20130	4.35	0.07
17790	3.56	0.08
16380	2.55	0.08
14670	4.35	0.09
11760	3.56	0.10
9570	4.35	0.11
7700	6.87	0.13
7300	2.55	0.13
6120	3.56	0.14
5130	6.87	0.15

The loop and wall temperatures are then recorded, and the sampling scoops advanced then retracted, one at a time, proceeding from bottom to top of the stainless steel tube, to determine the mean film temperatures.

Fig. 3(a)–(c) show photos of the test facility, top view of a scoop, and stainless steel tube and sampling scoops mounted on micrometer stages, respectively. Additional details about the experimental facility and measurement techniques can be found in [36,40].

3. Numerical methods

Flow profiles and heat transfer characteristics are predicted using the FLUENT Analysis System in the Toolbox of ANSYS Workbench 14.0.0 [45]. The complete analysis is performed in the Project Schematic of Workbench, including geometry creation, meshing, processing and post-processing. Shown in Fig. 4, the com-

putational domain is a 2-dimensional axisymmetric system that is comprised of the inlet reservoir, porous film distributor and the 1835-mm long annulus formed between the outer wall of the 25.4-mm test section and the Lexgard chamber. The annulus is assigned an outer radius for a flow area equal to the actual flow area between the test section wall and inner walls of the square Lexgard chamber. The 2-dimensional assumption is justified by the axisymmetric nature of the film flow and small ratio of film thickness to distance between the test section and walls of the Lexgard chamber. The standard two-equation *k*–*ε* turbulent model as prescribed in the ANSYS Guide [45] is used to predict two-dimensional flow profiles and heat transfer characteristics of the computational domain. Two-phase treatment follows the Volume of Fluid (VOF) model [46]. Solid–liquid interfaces are governed by continuities of both temperature and heat flux.

The governing equations are written for unsteady, turbulent and incompressible flow with constant properties. Using the turbulent flow nomenclature $u_x = \bar{u}_x + u'_x$, $u_r = \bar{u}_r + u'_r$, and $T = \bar{T} + T'$ for the fluid region, the time-averaged continuity, axial and radial momentum, and energy equations are expressed, respectively, as [47]

$$\frac{\partial \bar{u}_x}{\partial x} + \frac{1}{r} \frac{\partial (r \bar{u}_r)}{\partial r} = 0, \tag{6}$$

$$\rho \left(\frac{\partial \bar{u}_x}{\partial t} + \bar{u}_x \frac{\partial \bar{u}_x}{\partial x} + \bar{u}_r \frac{\partial \bar{u}_x}{\partial r} \right) = -\frac{\partial P}{\partial x} + 2 \frac{\partial}{\partial x} \left(\mu \frac{\partial \bar{u}_x}{\partial x} \right) + \frac{1}{r} \frac{\partial}{\partial r} \left(r \mu \left(\frac{\partial \bar{u}_x}{\partial r} + \frac{\partial \bar{u}_r}{\partial x} \right) \right) - \rho \left\langle \frac{\partial u'_x{}^2}{\partial x} + \frac{\partial (u'_x u'_r)}{\partial r} + \frac{u'_x u'_r}{r} \right\rangle + \rho g, \tag{7}$$

$$\rho \left(\frac{\partial \bar{u}_r}{\partial t} + \bar{u}_x \frac{\partial \bar{u}_r}{\partial x} + \bar{u}_r \frac{\partial \bar{u}_r}{\partial r} \right) = -\frac{\partial P}{\partial r} + \frac{\partial}{\partial x} \left(\mu \left(\frac{\partial \bar{u}_x}{\partial r} + \frac{\partial \bar{u}_r}{\partial x} \right) \right) + 2 \frac{1}{r} \frac{\partial}{\partial r} \left(r \mu \frac{\partial \bar{u}_r}{\partial r} \right) - 2 \mu \frac{\bar{u}_r}{r^2} - \rho \left\langle \frac{\partial (u'_x u'_r)}{\partial x} + \frac{\partial u'_r{}^2}{\partial r} + \frac{u'_r{}^2}{r} \right\rangle \tag{8}$$

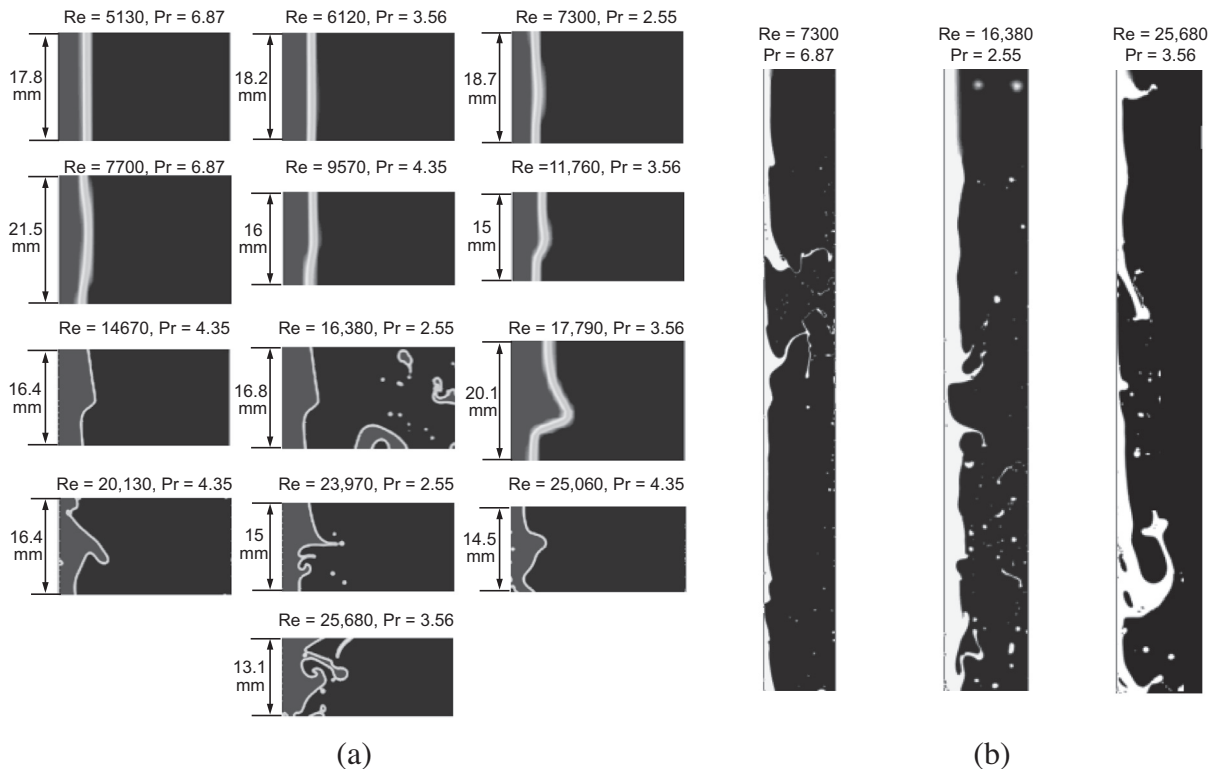


Fig. 5. (a) Dominant repeated wave shape for 13 test cases. (b) Variations of interfacial shape for 3 test cases.

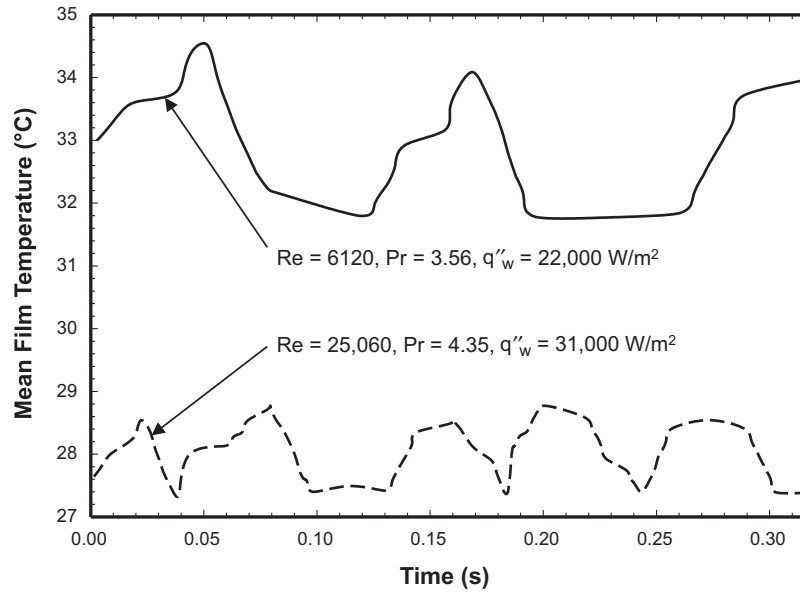


Fig. 6. Predicted temporal records of mean film temperature at $x = 350$ mm for two cases.

and

$$\frac{\partial \bar{T}}{\partial t} + \bar{u}_x \frac{\partial \bar{T}}{\partial x} + \bar{u}_r \frac{\partial \bar{T}}{\partial r} = \frac{\partial}{\partial x} \left(\alpha \frac{\partial \bar{T}}{\partial x} - \langle u'_x T' \rangle \right) + \frac{1}{r} \times \frac{\partial}{\partial r} \left(\alpha r \frac{\partial \bar{T}}{\partial r} - r \langle u'_r T' \rangle \right). \quad (9)$$

The fluctuating terms can be expressed in terms of the gradient of the mean quantities in accordance with the eddy viscosity hypothesis, where the eddy viscosity, μ_t , is expressed as

$$\mu_t = \frac{C_\mu \rho k^2}{\varepsilon}. \quad (10)$$

The kinetic energy and the dissipation energy equations are given, respectively, by

$$2\nabla \cdot \mu \langle \vec{\nabla} s_{ij} \rangle = \frac{\partial}{\partial x} \mu \left\{ \frac{\partial k}{\partial x} + \frac{\partial \langle u_x^2 \rangle}{\partial x} + \frac{1}{r} \frac{\partial r \langle u'_x u'_r \rangle}{\partial r} \right\} + \frac{1}{r} \times \frac{\partial}{\partial r} \mu r \left\{ \frac{\partial k}{\partial r} + \frac{\partial \langle u'_x u'_r \rangle}{\partial x} + \frac{1}{r} \frac{\partial r \langle u'_r{}^2 \rangle}{\partial r} \right\} \quad (11)$$

and

$$\varepsilon = \frac{2}{\rho} \mu \langle s_{ij} s_{ij} \rangle, \quad (12)$$

where

$$s_{ij} = \frac{\partial u'_r}{\partial x} + \frac{\partial u'_x}{\partial r}. \quad (13)$$

From an examination of turbulence models in Table 1, as well as an investigation of the value used in numerical turbulence modeling by Kays [48], a constant turbulent Prandtl number value of $Pr_t = 1$ is used. A numerical method to solving the present conjugate heat transfer problem is to treat the solid and fluid as a unitary computational domain and solve the above governing equations simultaneously (Patankar [49]). The boundary conditions are specified as follows. Velocity and liquid temperature in the reservoir inlet are assumed uniform and adjusted according to the desired Reynolds and Prandtl number, respectively: $U = \nu Re/D_H$, $V = 0$, and $T = T_{in}(Pr)$ for $x = -1060$ mm and -12.7 mm $\leq r \leq -6.6$ mm.

The porous film distributor has a porosity of 0.002 and a viscous resistance of 3.846×10^7 m⁻². Surface tension effects are considered at all walls. The outlet condition at the bottom of the domain is assumed to be uniform pressure equal to atmosphere, to conform to experimental conditions. Also to conform to the data, a constant heat flux is applied at the lower stainless steel portion of the test section that results in a temperature rise equal to that produced experimentally across the thermally-developed span of the film: $-k_s \partial T / \partial r = q''_w$ for $0 \leq x \leq 781$ mm.

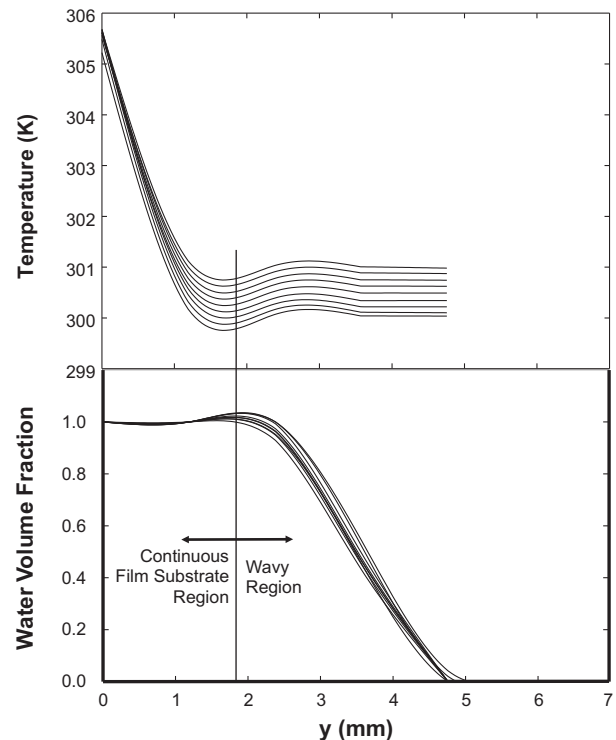


Fig. 7. Variations of film temperature profile at different subintervals within the period of a single dominant wave, and corresponding water volume fraction profiles for $x = 390.5$ mm, $Re = 25,060$, $Pr = 4.35$ and $q''_w = 55,000$ W/m².

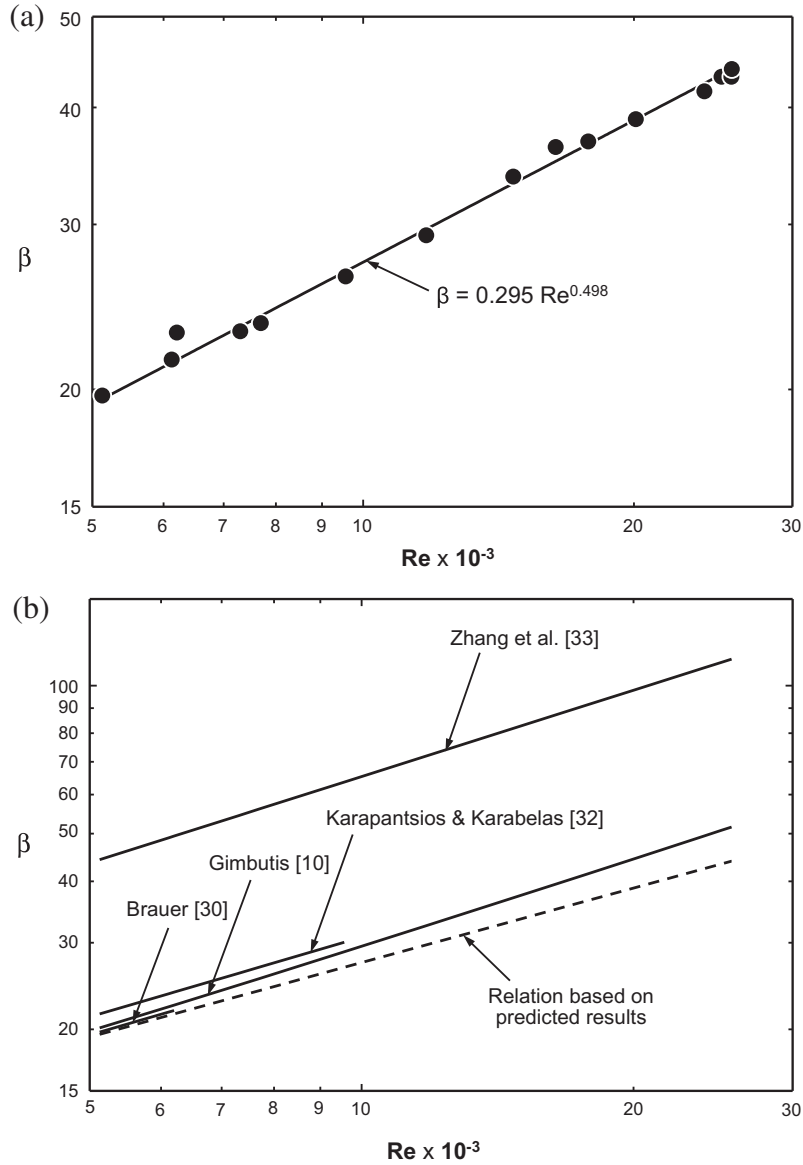


Fig. 8. (a) Curve fit to predicted film thickness for $Re = 5130\text{--}25,680$ and $Pr = 2.55\text{--}6.87$. (b) Comparison of present film thickness relation with prior correlations.

Although the vapor shear at the film interface is neglected, the influences of surface tension and molecular viscosity are considered. Hence, the tangential and normal force balance equations at the film surface are given, respectively, by

$$e_{ij}n_jt_i = 0 \tag{14}$$

and

$$-P + 2\mu e_{ij}n_jt_i = \sigma \left(\frac{1}{R_1} + \frac{1}{R_2} \right). \tag{15}$$

In order to conserve computation time, the fractional step version of the non-iterative time advancement (NITA) scheme is used with first-order implicit discretization at every time-step (Armsfield and Street [50]; Glaz et al. [51]) to obtain pressure-velocity coupling. Gradient generation during spatial discretization is accomplished using the least-squares cell-based scheme (Anderson and Bonhus [52]), while PRESTO, QUICK, Geo-reconstruct and first-order upwind schemes [53] are used for pressure, momentum, volume fraction and turbulent kinetic energy resolution, respectively.

The grid system consists of 401,426 nodes and 397,111 cells. Two other finer grid systems, with 633,612 and 781,344 cells,

showed minimal influence on computed values. Therefore, the coarser grid system is employed to reduce computation time and memory requirements. This grid is non-uniform, having a larger number of grid points near the wall, film interface, porous zone and heated portion of the test section in pursuit of superior accuracy in resolving key flow parameters. Although the bulk flow region of the falling film is modeled using the mesh size recommended for turbulence simulation, an order of magnitude refinement in the mesh is adopted beginning well outside the narrow viscous layer at the interface to ensure high resolution in capturing turbulence at the interface. This also ensures that the transition in refinement does not compromise the flow predictions.

4. Results

4.1. Influence of interfacial waves

To develop meaningful predictions of film thickness, heat transfer coefficient and eddy diffusivity, the process of computing turbulent parameters must be systematically laid out. First, the numerical simulation is run well into steady state for 13 test cases

that match experimental conditions; Re and Pr for these cases are listed in Table 4. Due to the wavy nature of the film, the location of the interface changes both spatially and temporally. The exact interface location has to be determined to facilitate the determination of local instantaneous as well as time averaged values for film thickness, temperature profile, heat transfer coefficient and eddy diffusivity profile. This location is especially important for accurate determination of eddy diffusivity since this is where turbulence dampening takes place.

Understanding the influence of interfacial waves is achieved for each axial location by repeating computations of water volume fraction for a sufficiently long time to ensure steady state conditions. At steady state, water volume fraction contour plots for the entire heated length are inspected to identify any repeatable wave patterns. This procedure is performed for all 13 test cases.

It is observed that each test case possesses a dominant repeated interfacial wave shape as shown in Fig. 5(a), where profile segments are shown over the entire y -span of the computational domain. However, for all the cases considered, an assortment of interfacial features other than the dominant wave shape are also encountered, three of which are shown in Fig. 5(b). Kostoglou et al. [54] characterized several of these features while studying large waves. Fig. 5(a) reveals that as Re increases, the waves become more chaotic, but the film's base substrate becomes thicker, an observation confirmed previously by Lyu and Mudawar [55]. This process of interfacial wave shape screening is carried out for various times and over the entire heated length. The dominant wave structure is examined at several discrete locations for local

turbulence and heat transfer characteristics, and these characteristics are used to generate local or averaged turbulence and heat transfer characteristics.

Determining the period Δt required to achieve steady state is achieved by examining temporal records of the heat transfer coefficient and computing local time averaged values of $\int_0^{\Delta t(x)} h_H(x,t) dt / \Delta t(x)$. The resulting Δt values are provided in Table 4. To further assess the validity of this time averaging technique, a sensitivity study is conducted relative to the magnitude of Δt . Using a Δt equal to the period of the dominant wave for the specific case considered gives time-averaged values of h_H close to the much longer steady state values. However, given the occasionally non-periodic nature of the interfacial waves, a Δt equal to the period of the dominant wave is deemed too short to ensure accurate time averaging. On the other hand, using a Δt 25 times the period of the dominant wave resulted in consistent and time-invariant prediction of h_H , and is therefore adopted throughout the study.

Fig. 6 sheds some light on the influence of interfacial waves on heat transfer across the film. Shown for two extreme test cases are temporal variations of the film's mean temperature. Notice that the two temporal records are fairly periodic. This type of plot is in fact very instrumental in determining both the wave period and Δt required for the aforementioned averaging of h_H . Fig. 6 shows the amplitude of temperature fluctuations decreases with increasing Re , an observation made earlier by Lyu and Mudawar [55] and attributed to both thicker substrate and enhanced turbulent mixing at high Re .

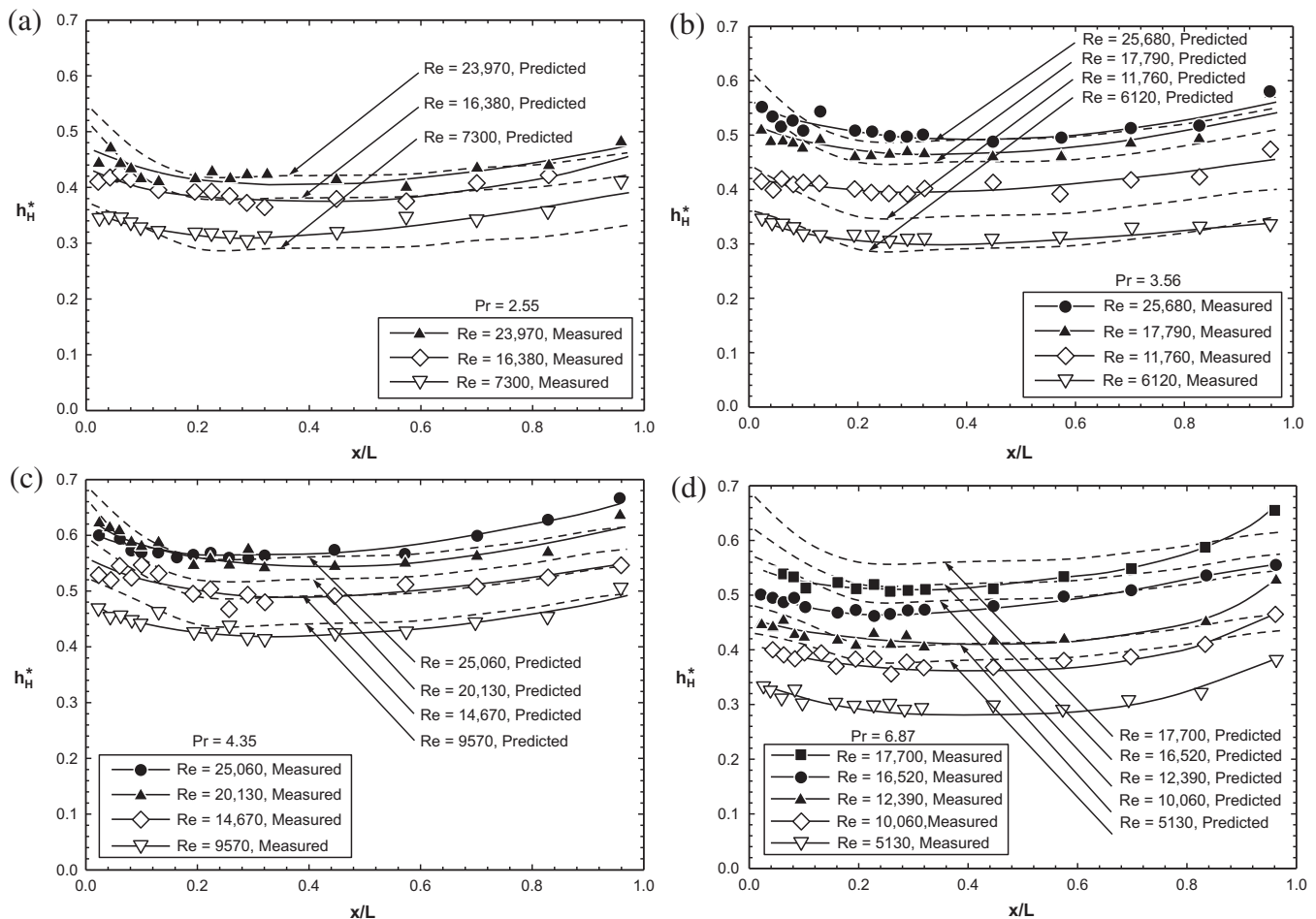


Fig. 9. Variations of measured and predicted dimensionless heat transfer coefficient along heated length of test section for (a) $Pr = 2.55$, (b) $Pr = 3.56$, (c) $Pr = 4.35$, and (d) $Pr = 6.87$.

To understand the temperature distribution from the wall to the interface, detailed temperature contour plots corresponding to the dominant wave profile are examined for one test case. As shown in Fig. 7, the liquid temperature is plotted versus distance from the wall at discrete locations within the period of one dominant wave. The computations are performed to produce a wall-to-mean temperature difference of 5°C, which is identical to that of the actual experiment. The corresponding water volume fraction plot is also shown to indicate the spans of the continuous liquid substrate and the wavy portion of the film. As expected, the temperature drops quickly within the continuous substrate of the film, then incurs a slight increase before reaching fairly uniform temperature within the wavy region. The temperature uniformity in the wavy region is indicative of strong mixing near the crests of the waves. This phenomenon has been previously explained by decomposing the liquid film into wavy and substrate regions [56].

4.2. Film thickness

For all 13 test cases included in Table 4, the time-averaged film thickness is computed along the heated length. The interface is detected by the distance from the heated wall where the calculated

water volume fraction drops to zero. For each set of conditions, the time averaging Δt for film thickness is identical to those used for h_H and indicated in Table 4. The computed thickness is averaged over the heated length and fitted by

$$\beta = 0.295Re^{0.498}, \tag{16}$$

as shown in Fig. 8(a), with a mean absolute error of 2.7%, maximum error of 11%, and standard deviation of 0.019. Fig. 8(b) compares Eq. (16) with predictions of prior falling film correlations provided in Table 2. Shown, for the range of test cases in Table 4, is fairly good agreement with the predictions of Brauer [30], Gimbutis [10], and Karapantsios and Karabelas [32], but with the correlation of Zhang et al. [33] displaying appreciable departure from all other predictions.

4.3. Heat transfer coefficient

Fig. 9(a)–(d) compare the predictions of h_H along the heated length L with measured values for $Pr = 2.55, 3.56, 4.35$ and 6.87 , respectively. Shown in each of these figures are predictions and data corresponding to a broad range of Re . The computations are performed at the exact Re and Pr values of the experiments, which

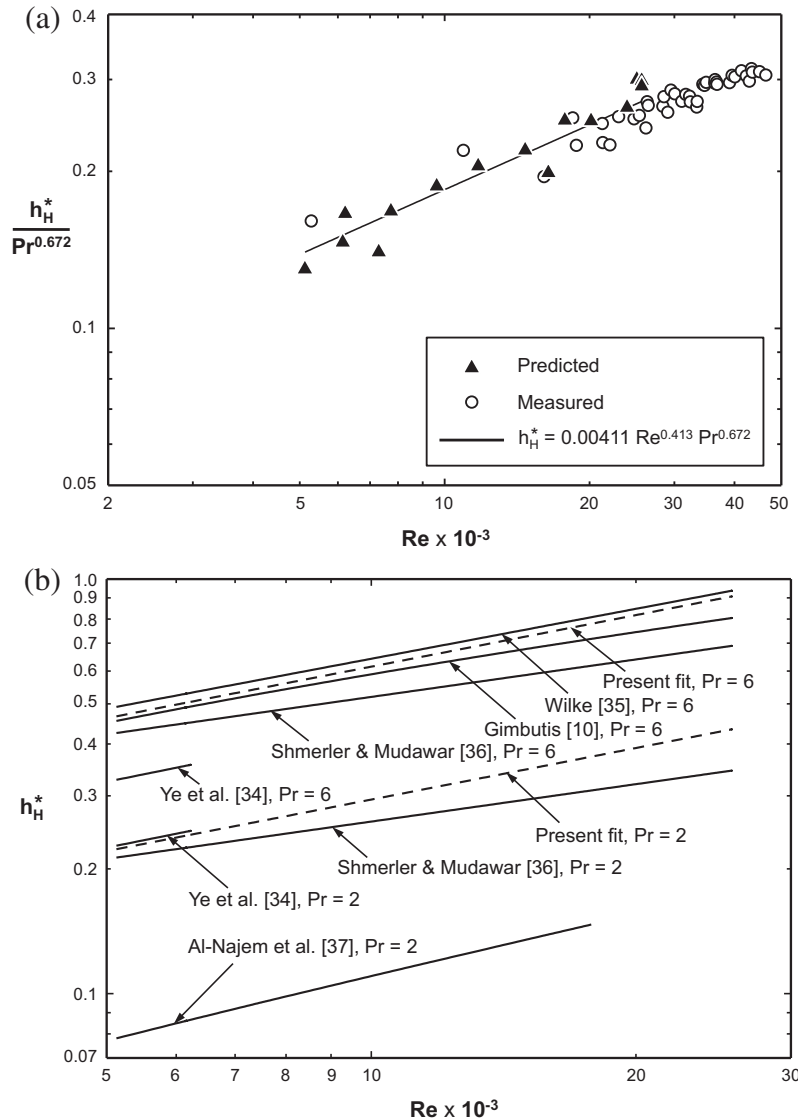


Fig. 10. (a) Comparison of measured and predicted heat transfer coefficient for $Re = 5130–25,680$ and $Pr = 2.55–6.87$. (b) Comparison of present heat transfer relation with prior correlations.

are listed in Table 4. However, predictions are excluded for certain extreme experimental test cases. On one extreme of very low Re , the flow through the porous film distributor could not produce a liquid film. For the other extreme of very high Re , severe turbulent fluctuations distort the flow to an extent that curtails film formation.

The predictions in Fig. 9(a)–(d) follow the data trends observed in Shmerler and Mudawar [36], featuring a gradual decrease in h_H over the upstream portion of the heated length, followed by a much slower increase over the remaining length. The upstream decrease can be directly attributed to initiation and development of the thermal boundary layer. The slight downstream increase can be explained by the slight thinning of the film, as proposed by Takahama and Kato [31] and Salazar and Marschall [57].

The dependence of the average heat transfer coefficient on Re and Pr is determined by curve-fitting the predictions shown in Fig. 9(a)–(d). For consistency with the experiments, the same methodology for determining the average value that was used in the experiments is also adopted for the numerical results. This involves determining the mean value from the longitudinal posi-

tion of minimum h_H to the next to last measurement position. Fig. 10(a) shows predicted values fitted to the function

$$h_H^* = 0.00411Re^{0.413} Pr^{0.672} \tag{17}$$

with a mean absolute error of 6.3%, maximum error of 21% and standard deviation of 0.038.

Fig. 10(b) compares, for $Pr = 2$ and 6, predictions of the heat transfer coefficient according to Eq. (17) with those of previous correlations, which are provided in Table 3. For $Pr = 2$, Eq. (17) matches well the predictions by Shmerler and Mudawar [36] and Ye et al. [34], while the correlation of Al-Najem et al. [37] shows appreciable deviation from the others. For $Pr = 6$, Eq. (16) shows good general agreement with the predictions of Wilke [35], Gimbutis [10], Shmerler and Mudawar, but the correlation by Yeh et al. provides much lower estimates than all others.

4.4. Eddy diffusivity profile

The dominant wave structure is examined at several discrete subintervals within the period of a single dominant wave to

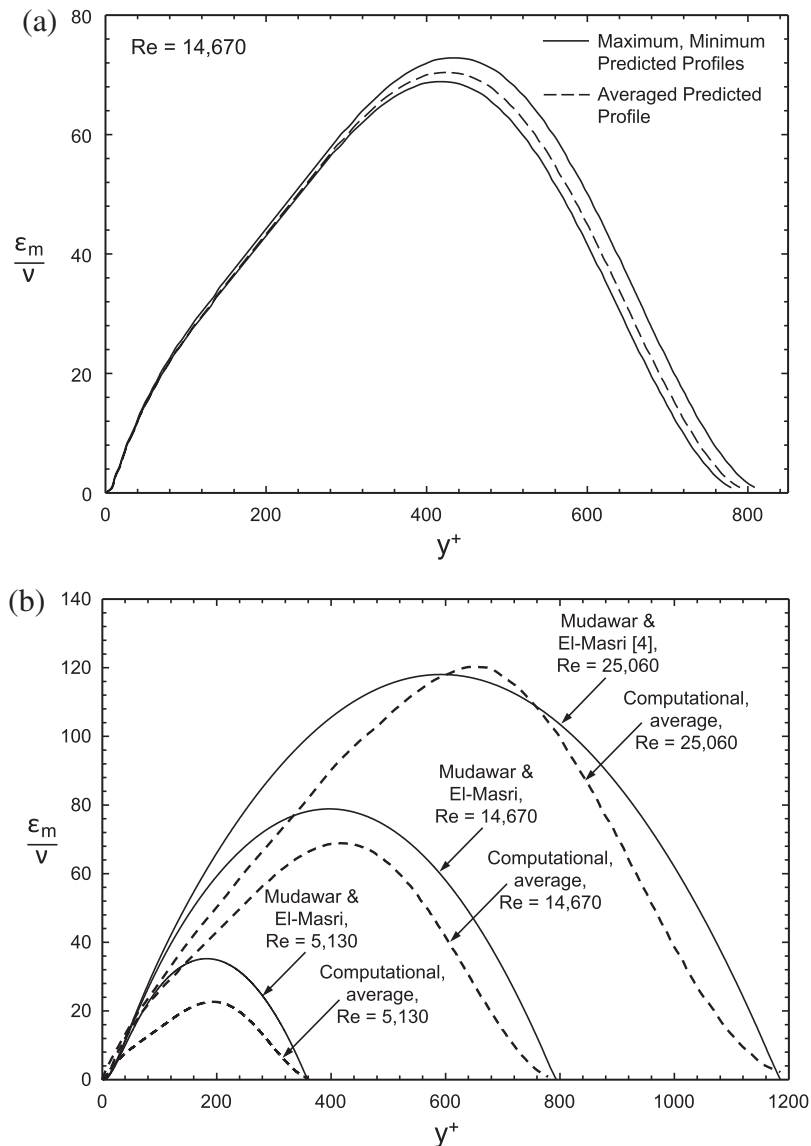


Fig. 11. (a) Maximum, minimum and average predicted eddy diffusivity profiles for $Re = 14,670$. (b) Comparison of predicted eddy diffusivity profile with Mudawar and El-Masri's [4] for $Re = 5,130, 14,670$ and $25,060$.

determine the variations of eddy diffusivity with y^+ . For each sub-interval, the corresponding plot of water volume fraction is consulted to confirm the location of the interface. These variations are then averaged to obtain the eddy diffusivity profile. Fig. 11(a) shows, for the dominant wave interval corresponding to $Re = 14,670$, the maximum, minimum and average eddy diffusivity profile. These plots clearly demonstrate that (i) eddy diffusivity is reduced to zero at the interface, and (ii) the shape of the eddy diffusivity profile resembles that of the continuous function recommended by Mudawar and El-Masri [4]. Fig. 11(b) compares the average profiles with predictions of Mudawar and El-Masri for three Reynolds numbers. Good agreement is achieved at $Re = 25,060$ and $14,670$, evidenced by R-square fits of 0.918 and 0.877, respectively. With a R-square fit of 0.802, the agreement is less accurate for the lowest Reynolds number of 5,130.

5. Conclusions

This study examined the influence of interfacial waves on heat transfer in turbulent, free-falling liquid films subjected to sensible heating, accounting for the interfacial dampening of turbulent eddies due to surface tension. Two-dimensional axisymmetric film flow on a vertical circular tube was modeled in Fluent, with both the computational domain and operating conditions matching those of an experimental database for water films. Key findings from the study are as follows.

1. Turbulent films are predicted to acquire a dominant repeated interfacial wave shape, which is interrupted by a far infrequent assortment of other more complex interfacial features. The waves become more chaotic with increasing Reynolds number, while the film's substrate grows thicker.
2. Liquid temperature is predicted to drop quickly within the continuous substrate of the film, then increase slightly before becoming fairly uniform within the wavy region because of strong mixing near the wave crests.
3. The predicted dimensionless film thickness dependence on Reynolds number agrees well with popular film correlations.
4. Variations of the heat transfer coefficient along the heated length predicted by the numerical model are in good agreement with the experimental data. Both predictions and experimental data show a gradual decrease in the heat transfer coefficient in the upstream region of the heated length, which is attributed to thermal boundary layer development, followed by a much slower increase over the remaining length, which is the result of intensified turbulence and interfacial waviness downstream.
5. The predicted dimensionless heat transfer coefficient dependence on Reynolds and Prandtl numbers agrees well with popular heat transfer coefficient correlations.
6. The model clearly demonstrates that turbulence is fully suppressed at the interface. The eddy diffusivity profile resembles the continuous function recommended by Mudawar and El-Masri [4] with good agreement in magnitude except for relatively low Reynolds numbers.

Acknowledgements

The authors are grateful for the partial support for this project from the National Aeronautics and Space Administration (NASA) under Grant No. NNX13AB01G.

References

- [1] W. Nusselt, Die oberflächenkondensation des wasserdampfes, VDI Z. 60 (1916) 541–569.
- [2] F.P. Incropera, D.P. Dewitt, Fundamentals of Heat and Mass Transfer, 5th ed., Wiley, New York, NY, 2002.
- [3] S.M. Yih, J.L. Liu, Prediction of heat transfer in turbulent falling liquid films with or without interfacial shear, AIChE J. 29 (1983) 284–295.
- [4] I. Mudawar, M.A. El-Masri, Momentum and heat transfer across freely-falling turbulent liquid films, Int. J. Multiphase Flow 12 (1986) 771–790.
- [5] A.E. Dukler, Fluid mechanics and heat transfer in vertical falling-film systems, Chem. Eng. Prog. 56 (1960) 1–10.
- [6] A. Iribarne, A.D. Gosman, D.B. Spalding, A theoretical and experimental investigation of diffusion-controlled electrolytic mass transfer between a falling film and a wall, Int. J. Heat Mass Transfer 10 (1967) 1661–1676.
- [7] H.R. Kunz, S. Yerazunis, An analysis of film condensation, film evaporation and single-phase heat transfer, ASME Paper No. 67-HT-1, 1967.
- [8] A.F. Mills, D.K. Chung, Heat transfer across turbulent falling films, Int. J. Heat Mass Transfer 16 (1973) 694–696.
- [9] H. Limberg, Wärmeübergang an turbulente und laminaire rieselfilme, Int. J. Heat Mass Transfer 16 (1973) 1691–1702.
- [10] G. Gimbutis, Heat transfer of a turbulent falling film, in: Proc. fifth Int. Heat Transfer Conf., Tokyo, Japan, vol. 2, 1974, pp. 85–89.
- [11] S. Ishigai, S. Nakanisi, M. Takehara, Z. Oyabu, Hydrodynamics and heat transfer of vertical falling liquid films (Part 2, analysis using heat transfer data), Bull. JSME 17 (1974) 106–113.
- [12] R.A. Seban, A. Faghri, Evaporation and heating with turbulent falling liquid films, J. Heat Transfer – ASME Trans. 98 (1976) 315–318.
- [13] G.L. Hubbard, A.F. Mills, D.K. Chung, Heat transfer across a turbulent falling film with concurrent vapour flow, J. Heat Transfer – ASME Trans. 98 (1976) 319–320.
- [14] F. Blangetti, R. Krebs, E. Schlunder, Condensation in vertical tubes—experimental results and modeling, Chem. Eng. Fundam. 1 (1982) 20–63.
- [15] O.C. Sandall, O.T. Hanna, C.L. Wilson, Heat transfer across turbulent falling films, AIChE Symp. Ser. 80 (1984) 3–9.
- [16] P.F. Peterson, V.E. Schrock, S.Z. Kuhn, Recent experiments for laminar and turbulent film heat transfer in vertical tubes, Nucl. Eng. Des. 175 (1997) 157–166.
- [17] A.A. Alhousseini, K. Tuzla, J.C. Chen, Falling film evaporation of single component liquids, Int. J. Heat Mass Transfer 41 (1998) 1623–1632.
- [18] A.A. Alhousseini, J.C. Chen, Transport phenomena in turbulent falling films, Ind. Eng. Chem. Res. 39 (2000) 2091–2100.
- [19] M. Asbik, O. Ansari, B. Zeghami, Numerical study of boundary layer transition in flowing film evaporation on horizontal elliptical cylinder, Numer. Heat Transfer 48 (2005) 645–669.
- [20] W.M. Rohsenow, J.H. Weber, A.T. Ling, Effect of vapour velocity on laminar and turbulent film condensation, Trans. ASME 78 (1956) 1637–1643.
- [21] R.G. Deissler, Turbulent heat transfer and friction in the entrance regions of smooth passages, Trans. ASME 78 (1955) 1221–1233.
- [22] D.B. Spalding, A single formula for the law of the wall, J. Appl. Mech. 83 (1961) 455–458.
- [23] E.R. Van Driest, On turbulent flow near a wall, J. Aerosp. Sci. 23 (1956) 1007–1011.
- [24] H. Ueda, R. Moller, S. Komori, T. Mizushima, Eddy diffusivity near the free surface of open channel flow, Int. J. Heat Mass Transfer 20 (1977) 1127–1136.
- [25] W.M. Kays, Heat transfer to the transported turbulent boundary layer, Int. J. Heat Mass Transfer 15 (1972) 1023–1044.
- [26] W.M. Kays, M.E. Crawford, Convective Heat and Mass Transfer, second ed., McGraw-Hill, New York, NY, 1980.
- [27] Y.S. Won, A.F. Mills, Correlation of the effects of viscosity and surface tension on gas absorption rates into freely falling turbulent liquid films, Int. J. Heat Mass Transfer 25 (1982) 223–229.
- [28] T. Von Karman, The analogy between fluid friction and heat transfer, Trans. ASME 61 (1939) 705–710.
- [29] H. Schlichting, Boundary-layer Theory, seventh ed., McGraw-Hill, New York, NY, 1979.
- [30] H. Brauer, Stromung und warmenübergang bei rieselfilmen, VDI Forschungsheft 457 (1956) 1–40.
- [31] H. Takahama, S. Kato, Longitudinal flow characteristics of vertically falling liquid films without concurrent gas flow, Int. J. Multiphase Flow 6 (1980) 203–215.
- [32] T.D. Karapantsios, A.J. Karabelas, Longitudinal characteristics of wavy falling films, Int. J. Multiphase Flow 21 (1995) 119–127.
- [33] J.T. Zhang, B.X. Wang, X.F. Peng, Falling liquid film thickness measurement by an optical-electronic method, Rev. Sci. Instrum. 71 (2000) 1883–1886.
- [34] X. Ye, W. Yan, Z. Jiang, C. Li, Hydrodynamics of free-falling turbulent wavy films and implications for enhanced heat transfer, Heat Transfer Eng. 23 (2002) 48–60.
- [35] W. Wilke, Wärmeübergang an rieselfilme, VDI Forschungsheft 490 (1962) 1–36.
- [36] J.A. Shmerler, I. Mudawar, Local heat transfer coefficient in wavy free-falling turbulent liquid films undergoing uniform sensible heating, Int. J. Heat Mass Transfer 31 (1988) 67–77.
- [37] N.M. Al-Najem, K.Y. Ezuddin, M.A. Darwish, Heat transfer analysis of preheated turbulent falling films in vertical tube evaporators, Desalination 115 (1998) 43–55.
- [38] B.G. Ganchev, V.M. Koglov, V.V. Lozovetskiy, Study of heat transfer to a falling fluid film at a vertical surface, Heat Transfer – Sov. Res. 4 (1972) 102–110.
- [39] G.J. Gimbutis, A.J. Drobacivius, S.S. Sinkunas, Heat transfer of a turbulent water film at different initial flow conditions and high temperature gradients, in: Proc. 6th Int. Heat Transfer Conf., Toronto, Canada, vol. 1, 1978, pp. 321–326.

- [40] J.A. Shmerler, I. Mudawar, Local evaporative heat transfer coefficient in turbulent free-falling liquid films, *Int. J. Heat Mass Transfer* 31 (1988) 731–742.
- [41] T.H. Lyu, I. Mudawar, Determination of wave-induced fluctuations of wall temperature and convection heat transfer coefficient in the heating of a turbulent falling liquid film, *Int. J. Heat Mass Transfer* 34 (1991) 2521–2534.
- [42] T.H. Lyu, I. Mudawar, Simultaneous measurement of thickness and temperature profile in a wavy liquid film falling freely on a heating wall, *Exp. Heat Transfer* 4 (1991) 217–233.
- [43] I. Mudawar, R.A. Houpt, Mass and momentum transport in smooth falling liquid films laminarized at relatively high Reynolds numbers, *Int. J. Heat Mass Transfer* 36 (1993) 3437–3448.
- [44] I. Mudawar, R.A. Houpt, Measurement of mass and momentum transport in wavy-laminar falling liquid films, *Int. J. Heat Mass Transfer* 36 (1993) 4151–4162.
- [45] ANSYS FLUENT 12.1 in Workbench User's Guide. ANSYS Inc., Canonsburg, PA, 2009.
- [46] C.W. Hirt, B.D. Nicholls, Volume of fluid (VOF) method for dynamics of free boundaries, *J. Comput. Phys.* 39 (1981) 201–225.
- [47] J.O. Hinze, *Turbulence*, McGraw-Hill, New York, NY, 1975.
- [48] W.M. Kays, Turbulent Prandtl number – where are we?, *J. Heat Transfer – Trans. ASME* 116 (1994) 284–295.
- [49] S.V. Patankar, A numerical method for conduction in composite materials, flow in irregular geometries and conjugate heat transfer. in: *Proc. third Int. Heat Transfer Conf.*, Toronto, Canada, vol. 3, 1978, pp. 297–302.
- [50] S. Armsfield, R. Street, The fractional-step method for the Navier–Stokes equations on staggered grids: accuracy of three variations, *J. Comput. Phys.* 153 (1999) 660–665.
- [51] H.M. Glaz, J.B. Bell, P. Colella, An analysis of the fractional-step method, *J. Comput. Phys.* 108 (1993) 51–58.
- [52] W. Anderson, D.L. Bonhus, An implicit algorithm for computing turbulent flows on unstructured grids, *Comput. Fluids* 23 (1994) 1–21.
- [53] S.V. Patankar, *Numerical Heat Transfer and Fluid Flow*, Hemisphere, Washington, DC, 1980.
- [54] M. Kostoglou, K. Samaras, T.D. Karapantsios, Large wave characteristics and their downstream evolution at high Reynolds number falling films, *AIChE* 56 (2010) 11–23.
- [55] T.H. Lyu, I. Mudawar, Statistical investigation of the relationship between interfacial waviness and sensible heat transfer to a falling liquid film, *Int. J. Heat Mass Transfer* 34 (1991) 1451–1464.
- [56] T. Karapantsios, M. Kostoglou, A.J. Karabelas, Local condensation rates of steam/air mixtures in direct contact with a falling liquid film, *Int. J. Heat Mass Transfer* 38 (1995) 779–794.
- [57] R.P. Salazar, E. Marschall, Time-averaged local thickness measurements in falling liquid film flow, *Int. J. Multiphase Flow* 4 (1978) 405–412.